

Plasmon spectrum and plasmon-mediated energy transfer in a multiconnected geometry

L. Shan, E. G. Mishchenko, and M. E. Raikh

Department of Physics and Astronomy, University of Utah, Salt Lake City, Utah 84112, USA

(Received 28 July 2015; revised manuscript received 5 February 2016; published 24 February 2016)

Surface plasmon spectrum of a metallic hyperbola can be found analytically with the separation of variables in elliptic coordinates. The spectrum consists of two branches: a symmetric, low-frequency branch, $\omega < \omega_0/\sqrt{2}$, and an antisymmetric high-frequency branch, $\omega > \omega_0/\sqrt{2}$, where ω_0 is the bulk plasmon frequency. The frequency width of the plasmon band increases with decreasing the angle between the asymptotes of the hyperbola. For the simplest multiconnected geometry of two hyperbolas separated by an air spacer the plasmon spectrum contains two low-frequency branches and two high-frequency branches. Most remarkably, the lower of the two low-frequency branches exists at $\omega \rightarrow 0$; i.e., unlike a single hyperbola, it is “thresholdless.” We study how the complex structure of the plasmon spectrum affects the energy transfer between two emitters located on the surface of the same hyperbola and on the surfaces of different hyperbolas.

DOI: [10.1103/PhysRevB.93.085435](https://doi.org/10.1103/PhysRevB.93.085435)

I. INTRODUCTION

The two central issues of contemporary plasmonics are manipulation and focusing of light on subwavelength scales, and plasmon-mediated energy transfer; see recent reviews Refs. [1–4].

With regard to the first issue, strong confinement of optical fields at small scales is accompanied by their orders-of-magnitude enhancement. This enhancement can be used, e.g., to boost nonlinear effects or to image and detect [5] small objects. At the core of the second issue is the light-matter interaction. The effect of the plasmon-supporting interface on a group of emitters located nearby [6–14] is twofold. First, it strongly modifies the radiative lifetimes of individual emitters. Second, virtual plasmon exchange facilitates the dipole-dipole interaction between emitters.

A metallic strip or a wire of finite thickness can serve as a plasmonic waveguide. The key approach to plasmon field focusing utilizes tapering, i.e., gradual narrowing of a waveguide towards one end [15–26]. Field confinement at the end of a tapered metal wire waveguide was demonstrated experimentally [4,27–29].

Current advances in plasmonics are related to engineering of progressively more complex plasmonic structures [30–35]. Then it is natural to extend the theoretical study of plasmonic waveguides to these complex, in particular, multiconnected, geometries, which contain several *disconnected* metal-air boundaries. It can be expected that these geometries provide additional control over plasmon fields. Studies of plasmons in multiconnected geometries should encompass calculation of the spectra of plasmonic modes as well as investigation of interaction of dipole emitters mediated by such modes.

Below we consider the simplest example of a multiconnected geometry, illustrated in Fig. 1. Geometries of a metallic “neck,” Fig. 1(a), and of two tapers separated by a narrow air “groove,” Fig. 1(b), are dual to each other. Both geometries possess a characteristic length scale $\sim a$, which is the size of the gap or the width of the constriction. This scale, being much smaller than all other scales in plasmonic structure, see Fig. 1(c), will therefore determine the plasmon spectrum and the plasmon field distribution of the entire structure.

We take advantage of the fact that the problem of calculation of the plasmon spectrum in geometry shown in Fig. 1 can

be solved exactly if the metallic surfaces are hyperbolic. A natural unit of momentum (wave number) is $q \sim a^{-1}$; the meaning of q in the absence of translational symmetry will be clarified below. One advantage of the analytical approach over numerical methods applied to concrete sets of parameters [37] is that an analytical solution allows us to establish general properties of the plasmon spectrum.

We compare the analytical results for two hyperbolas, Fig. 1, to the geometry of a single hyperbola. For a single hyperbola, the plasmon spectrum resembles the spectrum of a finite-width metallic strip. It consists of two branches: the low-frequency branch, $\omega < \omega_0/\sqrt{2}$, where ω_0 is the bulk plasmon frequency, corresponds to a symmetric mode, while the high-frequency branch, $\omega > \omega_0/\sqrt{2}$, corresponds to an antisymmetric mode. Adding the second hyperbola, Fig. 1, leads to the emergence of two additional branches in the plasmon spectrum. The frequency of the additional symmetric mode is lower than that for a single hyperbola, while the frequency of the additional antisymmetric mode is higher than a single hyperbola’s mode. Since the plasmons mediate the energy exchange between the emitters close to the surface, the complex plasmon structure in a multiconnected geometry leads to a nontrivial frequency dependence of this exchange, which we study analytically.

The paper is organized as follows. In Sec. II we present a detailed analysis of the plasmon spectrum and the field distribution of the plasmon modes in a single-hyperbola geometry. This analysis is then extended to the geometry of two hyperbolas in Sec. III. Excitation of plasmon modes by an emitter located at the metal boundary in a multiconnected geometry is studied in Sec. IV. Section V concludes the paper.

II. PLASMON SPECTRUM OF A SINGLE HYPERBOLA

A. Elliptic coordinates

We start with a single-hyperbola geometry, Fig. 2. The boundary of a metal is defined by the equation

$$\left(\frac{x}{\cos \eta_0}\right)^2 - \left(\frac{y}{\sin \eta_0}\right)^2 = a^2. \quad (1)$$

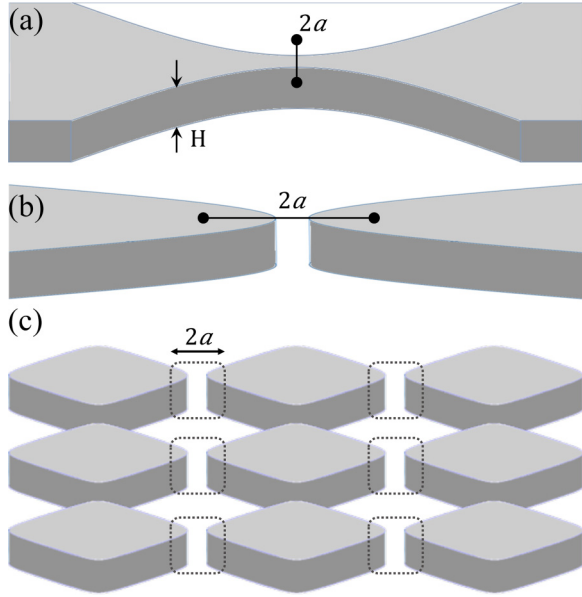


FIG. 1. Simplest examples of multiconnected plasmonic structures: (a) “neck” and (b) “gap.” The plasmon spectrum of these structures can be found analytically if metallic surfaces are confocal hyperbolas; $2a$ is the distance between the foci. (c) Schematic view of a plasmonic array [36]. The field distribution in the array is determined by the points of contact of metallic islands.

The metal is described with a dielectric permittivity,

$$\varepsilon(\omega) = 1 - \frac{\omega_0^2}{\omega^2}, \quad (2)$$

and occupies the inner part of the hyperbola, which approaches the asymptotes $y = \pm x \tan \eta_0$ at large x . Outside the hyperbola there is air with $\varepsilon = 1$.

Surface plasmons correspond to the solution of the Laplace equation, $\nabla(\varepsilon \nabla \Phi) = 0$, for the electrostatic potential, $\Phi(x, y)$, which propagates along the boundary of the hyperbola and

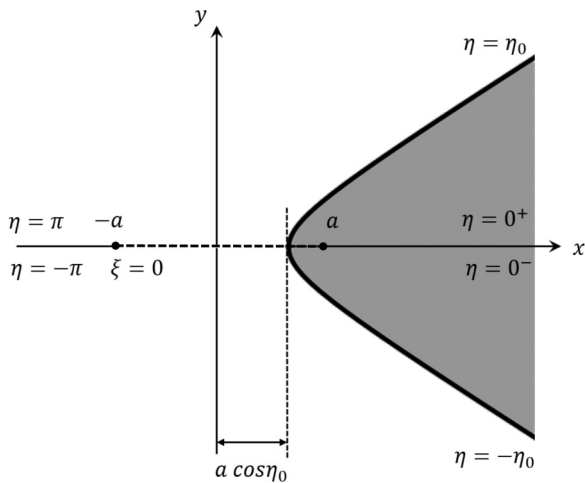


FIG. 2. Geometry of a single hyperbola. In elliptic coordinates ξ, η , defined by Eq. (3), the metal with dielectric constant, $\varepsilon(\omega)$, occupies the domain $(-\eta_0, \eta_0)$. Outside the hyperbola there is air with $\varepsilon = 1$.

decays away from the boundary. The variables in the 2D Laplace equation can be separated in elliptic coordinates

$$x = a \cosh \xi \cos \eta, \quad y = a \sinh \xi \sin \eta, \quad (3)$$

where ξ is positive and η changes in the interval $-\pi < \eta < \pi$. The Lamé coefficients are the same for both coordinates, $h_\xi = h_\eta = \sqrt{\cosh^2 \xi - \cos^2 \eta}$. In the new coordinates the Laplace equation,

$$\nabla^2 \Phi = \frac{1}{h_\xi^2} \left(\frac{\partial^2 \Phi}{\partial \xi^2} + \frac{\partial^2 \Phi}{\partial \eta^2} \right) = 0, \quad (4)$$

has a structure similar to its usual Cartesian form. The solutions of Eq. (4) should satisfy the boundary conditions at $\eta = \eta_0$ (upper half of the hyperbola) and at $\eta = -\eta_0$ (lower half of the hyperbola): the potential Φ and the normal component of the displacement field, $D_n = \varepsilon h_\xi^{-1} \partial \Phi / \partial \eta$, should be continuous at this boundary.

B. Plasmon dispersion

The geometry in Fig. 2 is symmetric with respect to the change of sign of the y axis. Correspondingly, the solutions of Eq. (4) can be classified into symmetric (even), $\Phi_s(x, y) = \Phi_s(x, -y)$, and antisymmetric (odd), $\Phi_a(x, y) = -\Phi_a(x, -y)$. In hyperbolic coordinates the reversal of the sign of y amounts to the change $\eta \rightarrow -\eta$, so that $\Phi_s(\xi, \eta) = \Phi_s(\xi, -\eta)$ and $\Phi_a(\xi, \eta) = -\Phi_a(\xi, -\eta)$.

Consider first the symmetric modes. For these modes, a general solution of Eq. (4) inside the hyperbola, $|\eta| < \eta_0$, which propagates along ξ and grows with η from $\eta = 0$ towards the boundary, has the form

$$\Phi_s(\xi, \eta) = A[\exp(im\xi) + \alpha \exp(-im\xi)] \cosh(m\eta). \quad (5)$$

In order to satisfy the continuity of the potential at $\eta = \pm\eta_0$, the corresponding solution outside the hyperbola, $|\eta| > \eta_0$, must have the same ξ dependence. It should also decay away from the boundary. This specifies the form of $\Phi_s(\xi, \eta)$ in the air:

$$\Phi_s(\xi, \eta) = B[\exp(im\xi) + \alpha \exp(-im\xi)] \cosh m(\pi - |\eta|). \quad (6)$$

By matching $\Phi_s(\xi, \eta)$ and $\varepsilon \partial \Phi_s / \partial \eta$ at the boundary $\eta = \pm\eta_0$, we obtain the dispersion equation for the symmetric modes:

$$\varepsilon(\omega) \tanh(m\eta_0) \coth[m(\pi - \eta_0)] = -1. \quad (7)$$

At first glance it appears that the constant α in Eqs. (5) and (6) can be arbitrary. However, from the requirement that the function $\Phi_s(\xi, \eta)$ be finite and continuous it follows that $\alpha = 1$. Indeed, for any $\alpha \neq 1$ the ξ component of electric field, $E_\xi = -h_\xi^{-1} \partial \Phi_s / \partial \xi$, diverges when $\xi \rightarrow 0$ and $\eta \rightarrow 0$, since the Lamé coefficient h_ξ vanishes there. We thus conclude that $\Phi_s(\xi) \propto \cos(m\xi)$.

Consideration for antisymmetric modes proceeds along the same lines. It is not difficult to see that the solution $\cos(m\xi) \sinh(m\eta)$ must be discarded as discontinuous across the region of the x axis, where $-a < x < a$ and $\xi = 0$: the odd character of $\sinh(m\eta)$ with respect to $\eta \rightarrow -\eta$ implies that it can only be multiplied by a function of ξ that vanishes at $\xi = 0$. This suggests the following form of the potential,

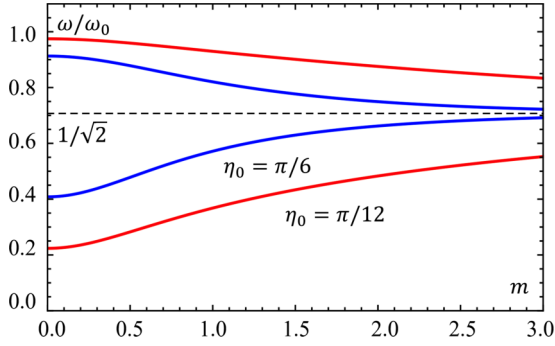


FIG. 3. Plasmon spectrum of a single hyperbola for two opening angles $2\eta_0 = \pi/10$ (red) and $2\eta_0 = \pi/3$ (blue) is plotted from Eq. (11) for a symmetric mode and Eq. (12) for antisymmetric mode. At large wave number, m , both branches approach the flat surface plasmon frequency, $\omega_0/\sqrt{2}$.

$\Phi_a(\xi, \eta)$, for antisymmetric modes inside the hyperbola:

$$\Phi_a(\xi, \eta) = C \sin(m\xi) \sinh(m\eta). \quad (8)$$

Correspondingly, the potential outside the hyperbola, which is odd with respect to y and matches the ξ dependence of Eq. (8), has the form

$$\Phi_a(\xi, \eta) = D \sin(m\xi) \sinh m(\pi - |\eta|). \quad (9)$$

The resulting dispersion equation for antisymmetric modes is

$$\varepsilon(\omega) \coth(m\eta_0) \tanh[m(\pi - \eta_0)] = -1. \quad (10)$$

From Eqs. (7) and (10) we can express the plasmon frequencies in terms of the dimensionless wave number m ,

$$\omega_s(m) = \omega_0 \left\{ \frac{\sinh(m\eta_0) \cosh[m(\pi - \eta_0)]}{\sinh(m\pi)} \right\}^{1/2}, \quad (11)$$

$$\omega_a(m) = \omega_0 \left\{ \frac{\cosh(m\eta_0) \sinh[m(\pi - \eta_0)]}{\sinh(m\pi)} \right\}^{1/2}. \quad (12)$$

Examples of dispersions Eqs. (11) and (12) are shown in Fig. 3. Below we list some general properties of these dispersions:

(i) A hyperbola reduces to a plane for $\eta_0 = \pi/2$. Then Eqs. (11) and (12) reproduce the expected result, $\omega_s(m) = \omega_a(m) = \omega_0/\sqrt{2}$, for the frequency of a dispersionless surface plasmon.

(ii) The spectra Eqs. (11) and (12) of the symmetric and antisymmetric modes satisfy the “sum rule” relation,

$$\omega_s^2(m) + \omega_a^2(m) = \omega_0^2. \quad (13)$$

(iii) In the long-wavelength limit, $m \rightarrow 0$, the threshold frequencies are

$$\omega_s(0) = \omega_0 \left(\frac{\eta_0}{\pi} \right)^{1/2}, \quad \omega_a(0) = \omega_0 \left(1 - \frac{\eta_0}{\pi} \right)^{1/2}. \quad (14)$$

The fact that $\omega_s(0)$ goes to zero for small η_0 could be expected, since at small η_0 the hyperbola is effectively a metallic layer with zero thickness, for which the dispersion of the longitudinal surface plasmon does not have a threshold [38]. On the other hand, ω_a approaching ω_0 for $\eta_0 \rightarrow 0$ can be interpreted by noticing that the oscillations of the electron

density, accompanying this plasmon, are normal to the surface; such oscillations must have the bulk-plasmon frequency ω_0 .

(iv) Another notable property of the dispersions Eqs. (11) and (12) is their *duality*, namely,

$$\omega_s(\pi - \eta_0, m) = \omega_a(\eta_0, m). \quad (15)$$

Qualitative interpretation of this relation can be given for small η_0 , when Eq. (15) relates the spectrum of a sharp metal “edge” with the spectrum of a narrow “funnel”: it suggests that the frequency of a soft symmetric plasmon of the “edge” coincides with the frequency of an antisymmetric plasmon in a “funnel.” Indeed, once the plasmon frequency is low, the absolute value of $\varepsilon(\omega)$ is big. This, in turn, implies that the normal component of the oscillating electric field in the metal is small. In the funnel geometry, this small field amplitude can be realized only when *opposite* charges accumulate on the two surfaces of the funnel. The reason is that, for a small-angle funnel, such antisymmetric arrangement is similar to the charges of a parallel-plate capacitor; this distribution of charges ensures that the field of the parallel-plate capacitor does not extend outwards. On the other hand, as we mentioned above, the low-frequency plasmon in a sharp-edge geometry is longitudinal, which corresponds to *symmetric* amplitudes of the charge-density fluctuations for the two surfaces.

C. Field distribution

In addition to the spectrum, $\omega(m)$, it is instructive to look at the spatial distribution of the electric field of the two plasmon modes. For a given frequency, ω , the value of m is found by equating it to either $\omega_s(m)$, when $\omega < \omega_0/\sqrt{2}$, or to $\omega_a(m)$, when $\omega > \omega_0/\sqrt{2}$. The found value of $m(\omega)$ is then substituted into the potential distribution $\Phi_s = \cos(m\xi) \cosh(m\eta)$ or $\Phi_a = \sin(m\xi) \sinh(m\eta)$, from which the electric field is subsequently calculated.

To clarify the physical meaning of the parameter m we rewrite the potential Φ_s at large distances from the coordinate origin in the Cartesian coordinates:

$$\Phi_s(x, y)|_{x, y \gg a} = C \cos \left[m \left(\ln \frac{2\sqrt{x^2 + y^2}}{a} \right) \right] \times \cosh \left[m \arctan \frac{y}{x} \right]. \quad (16)$$

The ratio of the amplitudes of Φ_s at the boundary, $y = x \tan \eta_0$, and along the x axis is equal to $\cosh(m\eta_0)$.

The potential distribution Eq. (16) applies inside the metal. In the air, this distribution differs from Eq. (16) by the replacement $\arctan(\frac{y}{x})$ by $\pi - \arctan(\frac{y}{x})$ and C by $C \cosh(m\eta_0) / \cosh[m(\pi - \eta_0)]$.

Consider now a symmetric plasmon propagating with a wave vector, q , in a metallic film of a constant thickness, $2d$. For this plasmon the ratio of the potentials at the boundary and at the center is equal to $\cosh(qd)$. Identifying d with the length of the arc between the x axis and the boundary, $\rho\eta_0$, where $\rho = \sqrt{x^2 + y^2}$, allows one to specify the local value of the wave vector,

$$q(\rho) = \frac{m}{\rho}. \quad (17)$$

With the ρ -dependent wave vector given by Eq. (17), one would expect for the plasmon phase a “semiclassical” value $\int_a^\rho d\rho' q(\rho') = m \ln(\rho/a)$, which is indeed the case, as follows from Eq. (16).

For a symmetric mode, the electric field on the x axis is directed along x . The domain $x > a$ on the x axis corresponds to $\eta = 0$, so that $\Phi_s(\xi) = C \cos(m\xi)$. In this domain the behavior of electric field with $x = a \cosh \xi$ has the form

$$E_x(x > a) = Cm \frac{\sin \left[m \ln \left(\frac{x}{a} + \sqrt{\frac{x^2}{a^2} - 1} \right) \right]}{\sqrt{x^2 - a^2}}. \quad (18)$$

The field is finite at $x = a$, and falls off as $1/x$ for $x \gg a$.

In the domain $a \cos \eta_0 < x < a$ we have $\xi = 0$ and $\Phi_s = C \cosh(m\eta)$. Differentiating with respect to $x = a \cos \eta$, we obtain

$$E_x(a \cos \eta_0 < x < a) = Cm \frac{\sinh \left(m \arccos \frac{x}{a} \right)}{\sqrt{a^2 - x^2}}. \quad (19)$$

Finally, in the air, in the domain $0 < x < a \cos \eta_0$ the x component of the field is given by

$$E_x(0 < x < a \cos \eta_0) = -mC \left(\frac{\cosh(m\eta_0)}{\cosh[m(\pi - \eta_0)]} \right) \frac{\sinh \left[m \left(\pi - \arccos \frac{x}{a} \right) \right]}{\sqrt{a^2 - x^2}}. \quad (20)$$

In Eqs. (18) and (19) the frequency and the η_0 dependence of the electric field are incorporated in $m(\omega, \eta_0)$, defined by the condition $\omega_s(m) = \omega$, where $\omega_s(m)$ is given by Eq. (11).

For an antisymmetric mode, the electric field on the x axis is directed along y . Inside the metal, where $\Phi_a = C \sin(m\xi) \sinh(m\eta)$, the x dependence of E_y is the same as the x dependence, Eqs. (19) and (20), of E_x for the symmetric mode. In the air, the x dependence of E_y is different from Eq. (20) and has the form

$$E_y(0 < x < a \cos \eta_0) = -mC \left(\frac{\sinh(m\eta_0)}{\sinh[m(\pi - \eta_0)]} \right) \frac{\sinh \left[m \left(\pi - \arccos \frac{x}{a} \right) \right]}{\sqrt{a^2 - x^2}}. \quad (21)$$

The behavior of $E_x(x)$ and $E_y(x)$ is illustrated in Fig. 4(a). It is seen that the oscillating tail emerges only at large distance $\sim 20a$ from the tip.

It is possible to understand the difference in the distribution of the field intensities for symmetric and antisymmetric modes from simple qualitative arguments. As seen from Fig. 5, at small momenta, the field of the symmetric mode is predominantly concentrated outside the metal [39,40]. In contrast, the field of the antisymmetric mode is predominantly concentrated inside the metal. This difference can be traced to the continuity of the normal component of the displacement vector at the boundary: $E_\eta^{\text{(out)}} = \varepsilon(\omega) E_\eta^{\text{(in)}}$. For small m , the frequency of the symmetric mode is low, so that $|\varepsilon(\omega)| \gg 1$. Therefore, the field inside the material is much weaker than the field outside. Conversely, the frequency of the antisymmetric mode is close to ω_0 . As a result, $\varepsilon(\omega)$ is small for that mode, effectively reversing the relation of the fields inside and outside.

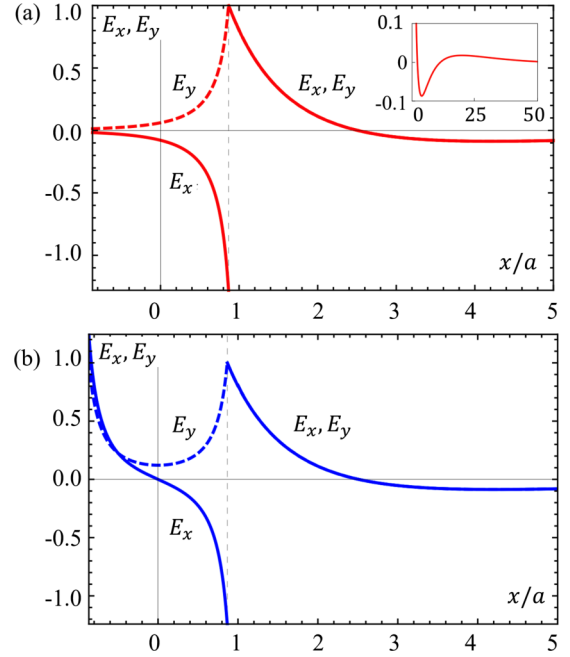


FIG. 4. (a) Distribution of E_x (for a symmetric mode) and E_y (for antisymmetric mode), the components of electric field along the x axis, is plotted from Eqs. (18)–(21) for the wave number $m = 2$ and the opening angle $2\eta_0 = \pi/3$. The inset shows the large- x oscillating tail of E_x . (b) The same as (a) for two hyperbolas.

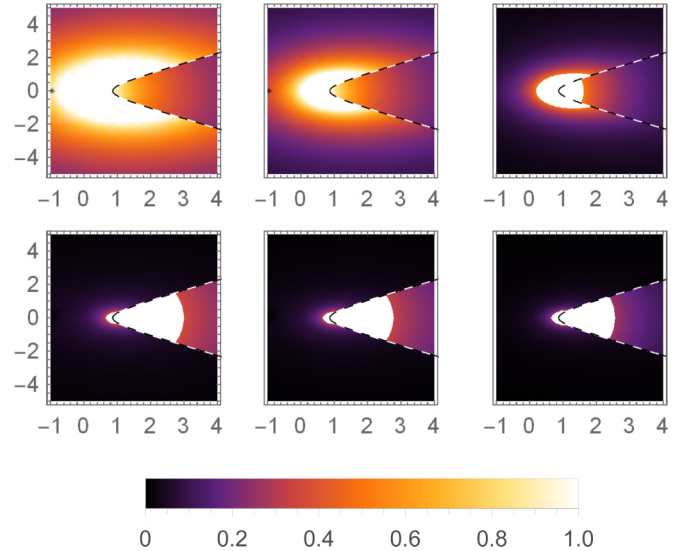


FIG. 5. Density plot of the field intensity of the plasmon modes for a single hyperbola with the opening angle $2\eta_0 = \pi/3$. The upper row corresponds to a symmetric mode, for which the potential distribution is determined by Eqs. (5) and (6). The lower row corresponds to an antisymmetric mode with the potential described by Eqs. (8) and (9). Left, central, and right panels correspond to the wave numbers $m = 0.1$, $m = 0.4$, and $m = 0.7$, respectively. With increasing m the plasmon frequencies approach $\omega_0/\sqrt{2}$, while the field concentrates near the metal-air surface.

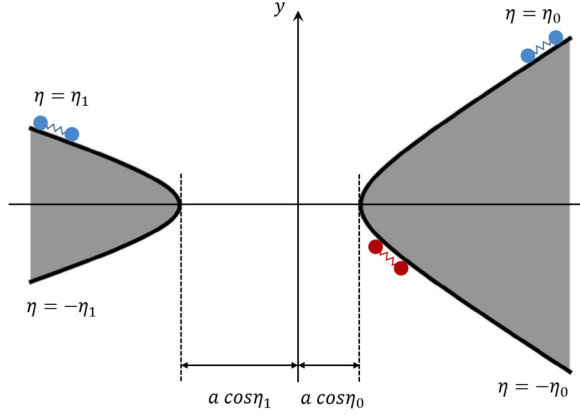


FIG. 6. The geometry of two hyperbolas with the opening angles $2\eta_0$ and $2\eta_1$. A dipole emitter close to the tip and polarized along the interface excites the dipoles located to the left and to the right from the tip at distances much greater than the focal distance.

III. GEOMETRY OF TWO HYPERBOLAS

A. Splitting of the plasmon spectrum

Consider now the geometry of two hyperbolas, Fig. 6. The boundary of the first hyperbola is defined by the same Eq. (1); in addition, metal occupies the domain $\pi - \eta_1 < \eta < \pi$. The ξ dependence of the potential for the symmetric modes remains the same, $\cos m\xi$. The η dependence, which decays away from both boundaries, is characterized by four constants,

$$\Phi_s(\eta) = \begin{cases} A_1 \cosh(m\eta), & 0 < \eta < \eta_0, \\ B_1 \cosh(m\eta) + B_2 \cosh m(\pi - \eta), & \eta_0 < \eta < \pi - \eta_1, \\ A_2 \cosh m(\pi - \eta), & \pi - \eta_1 < \eta < \pi. \end{cases} \quad (22)$$

These constants, A_1 , A_2 , B_1 , and B_2 , are related by continuity of $\Phi_s(\eta)$ and $\varepsilon \partial \Phi_s / \partial \eta$ at $\eta = \eta_0$ and $\eta = \pi - \eta_1$. These continuity conditions read

$$\begin{aligned} A_1 \cosh(m\eta_0) &= B_1 \cosh(m\eta_0) + B_2 \cosh m(\pi - \eta_0), \\ \varepsilon(\omega) A_1 \sinh(m\eta_0) &= B_1 \sinh(m\eta_0) - B_2 \sinh m(\pi - \eta_0), \end{aligned} \quad (23)$$

$$\begin{aligned} A_2 \cosh(m\eta_1) &= B_1 \cosh m(\pi - \eta_1) + B_2 \cosh(m\eta_1), \\ -\varepsilon(\omega) A_2 \sinh(m\eta_1) &= B_1 \sinh m(\pi - \eta_1) - B_2 \sinh(m\eta_1). \end{aligned} \quad (24)$$

These relations, together with the explicit form of $\varepsilon(\omega)$, given in Eq. (2), lead to the following characteristic equation:

$$\begin{aligned} & \frac{\sinh 2m\eta_0 \sinh 2m\eta_1}{4} \\ &= \left[\left(\frac{\omega^2}{\omega_0^2} - \frac{1}{2} \right) \sinh m\pi + \frac{1}{2} \sinh m(\pi - 2\eta_0) \right] \\ & \quad \times \left[\left(\frac{\omega^2}{\omega_0^2} - \frac{1}{2} \right) \sinh m\pi + \frac{1}{2} \sinh m(\pi - 2\eta_1) \right]. \end{aligned} \quad (25)$$

The two brackets on the right-hand side describe the plasmon dispersion Eq. (11) for a symmetric mode, while the left-hand side describes the coupling of the two plasmon branches. The two plasmons decouple when η_1 is small. Then the dispersion of the upper symmetric branch is simply $\omega_s(\eta_0, m)$, Eq. (11). In order to find the dispersion of the lower symmetric branch, it is sufficient to set $\omega = 0$ in the first bracket. This yields

$$\omega_s^-(m)|_{\eta_1 \ll 1} = \omega_0 [m\eta_1 \tanh m(\pi - \eta_0)]^{1/2}. \quad (26)$$

The general expression for the dispersion of the two coupled symmetric branches reads

$$\begin{aligned} \omega_s^\pm(m) &= \frac{\omega_0}{[2 \sinh(m\pi)]^{1/2}} \{ [\sinh(m\eta_0) \cosh m(\pi - \eta_0) \\ &+ \sinh(m\eta_1) \cosh m(\pi - \eta_1)] \\ &\pm [\sinh^2 m(\eta_0 - \eta_1) \cosh^2 m(\pi - \eta_0 - \eta_1) \\ &+ \sinh(2m\eta_0) \sinh(2m\eta_1)]^{1/2} \}^{1/2}. \end{aligned} \quad (27)$$

It is easy to see from Eq. (27) that for large $m \gg 1$ both frequencies approach the surface plasmon frequency $\omega_0/\sqrt{2}$, as in the case of a single hyperbola. The reason is that the short-wavelength plasmon is “local,” a metal surface is locally flat, and the presence of the second surface is of no consequence to the spectrum in this limit. The behavior of $\omega_s^\pm(m)$ in the limit of long wavelengths is remarkable:

$$\begin{aligned} \omega_s^-(m)|_{m \rightarrow 0} &\approx m\omega_0 \left[\frac{\eta_0 \eta_1 (\pi - \eta_0 - \eta_1)}{\eta_0 + \eta_1} \right]^{1/2}, \\ \omega_s^+(0) &= \omega_0 \left(\frac{\eta_0 + \eta_1}{\pi} \right)^{1/2}. \end{aligned} \quad (28)$$

The fact that $\omega_s^+(0)$ is determined by the “net” angle $(\eta_0 + \eta_1)$ is consistent with the result Eq. (14) for a single hyperbola. As this net angle approaches π , the portion of air in this limit becomes small, and $\omega_s^+(0)$ approaches the bulk plasmon frequency. The acoustic behavior of $\omega_s^-(m)$ is related to the fact that, unlike for a single hyperbola, in the geometry of two hyperbolas a low-frequency plasmon is not reflected from the tip, but goes “through” the gap into the second hyperbola.

For two identical hyperbolas, $\eta_0 = \eta_1$, Eq. (27) simplifies to

$$\begin{aligned} \omega_s^\pm(m) &= \omega_0 \left\{ \frac{\sinh(m\eta_0) \{ \cosh[m(\pi - \eta_0)] \pm \cosh(m\eta_0) \}}{\sinh(m\pi)} \right\}^{1/2}. \end{aligned} \quad (29)$$

Similar derivation for the antisymmetric plasmons yields

$$\begin{aligned} \omega_a^\pm(m) &= \omega_0 \left\{ \frac{\cosh(m\eta_0) \{ \sinh[m(\pi - \eta_0)] \pm \sinh(m\eta_0) \}}{\sinh(m\pi)} \right\}^{1/2}. \end{aligned} \quad (30)$$

From Eqs. (22), (30) one can trace the evolution of the plasmon spectrum with increasing η_0 . For $\eta_0 \ll 1$ the frequencies of

both symmetric plasmons are low:

$$\omega_s^-(m)|_{\eta_0 \ll 1} \approx \omega_0 \left[m \eta_0 \tanh\left(\frac{m\pi}{2}\right) \right]^{1/2}, \quad (31)$$

$$\omega_s^+(m)|_{\eta_0 \ll 1} \approx \omega_0 \left[\frac{m \eta_0}{\tanh\left(\frac{m\pi}{2}\right)} \right]^{1/2}, \quad (32)$$

while the frequencies of antisymmetric plasmons are close to ω_0 . As η_0 increases and achieves the value $\pi/4$, the branches $\omega_s^+(m)$ and $\omega_a^-(m)$ collapse into a single frequency $\omega_0/\sqrt{2}$ and become flat. As η_0 increases further above $\pi/4$, the branches invert: $\omega_s^+(m)$ is pushed above $\omega_0/\sqrt{2}$ and $\omega_a^-(m)$ drops below it. This evolution is illustrated in Fig. 8.

For the geometry of two hyperbolas there is a duality relation,

$$\omega_s^+\left(\frac{\pi}{2} - \eta_0, m\right) = \omega_a^-(\eta_0, m), \quad (33)$$

similar to Eq. (15) for a single hyperbola.

B. Comparison of the field distributions for two geometries

Hybridization of plasmon fields of individual hyperbolas in the geometry of two hyperbolas is illustrated in Figs. 4, 5, and 7. The curves in Fig. 4 suggest that hybridization *along the x axis* is rather weak and becomes progressively weaker while the wave number increases as the frequency approaches $\omega_0/\sqrt{2}$. This behavior is natural, since, the closer the frequency is to that of the flat surface plasmon, the more localized is the

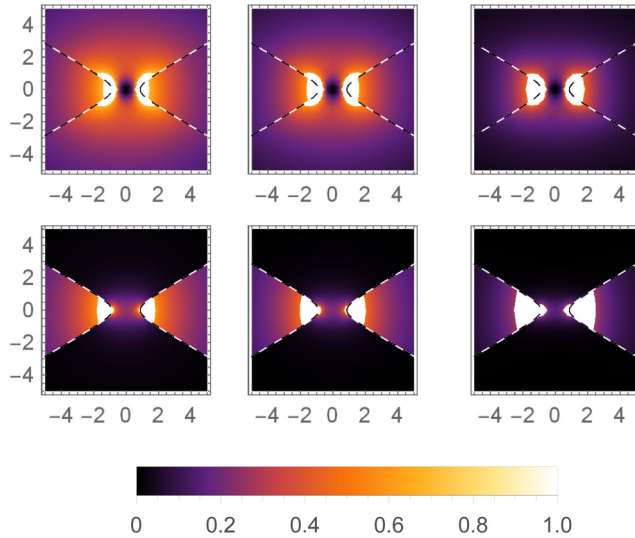


FIG. 7. Density plot of the field intensity of the plasmon modes in the geometry of two symmetric hyperbolas with the same opening angle, $2\eta_0 = \pi/3$, as in Fig. 5. The upper row corresponds to a symmetric mode for which the potential distribution is determined by Eqs. (22) and (27). Left, central, and right panels correspond, respectively, to the wave numbers $m = 0.1$, $m = 0.4$, and $m = 0.7$, the same as in Fig. 5. While the fields of individual hyperbolas are disconnected along the x axis, they overlap along the y axis. The lower row corresponds to antisymmetric modes with the same m values. The fields of individual hyperbolas overlap, predominantly, along the y axis.

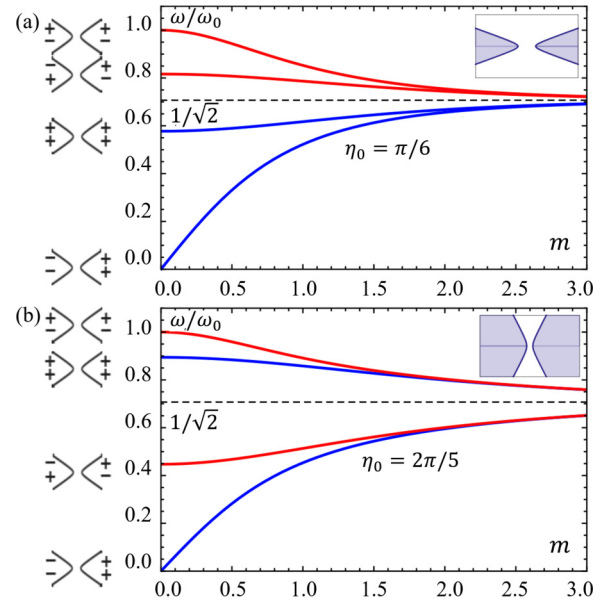


FIG. 8. Upper panel: Comparison of the plasmon spectra in the geometry of two hyperbolas for two values of the opening angle. For $\eta_0 = \pi/6 < \pi/4$ the frequencies of both symmetric modes (blue) are smaller than the flat surface plasmon frequency $\omega_0/\sqrt{2}$, while the frequencies of both antisymmetric modes (red) are bigger than $\omega_0/\sqrt{2}$. The relative signs of the oscillating charge density along the metal surfaces are schematically illustrated to the left of the graph. For $\eta_0 = 2\pi/5 > \pi/4$ (lower panel) the positions of the upper symmetric mode and lower antisymmetric mode with respect to ω_0 invert.

plasmon field near the metal-air interface. The density plot of the modes of individual hyperbolas is shown in Fig. 5. Compared with the latter, the double-hyperbola plot of Fig. 7 demonstrates that hybridization of individual modes has a “ring”-like character for symmetric modes and the “needle”-like character for antisymmetric modes. Such different nature of hybridization can be interpreted with the help of the patterns of oscillating surface charges in Fig. 8. For the bottom symmetric mode with low frequency, the positive and negative charges are separated by air, whereas the dielectric function of the metal is large. This expels the electric field lines from the inside of the metal and forces them to go through the air. The field is strong along the y axis, where it is parallel to the x axis.

For the antisymmetric mode, the upper and lower sides of the metal have opposite charges, while the frequency is close to ω_0 , so that the dielectric constant of the metal is small. The force lines of electric field are localized inside the metal. Thus, the two metal edges can be viewed as the plates of a parallel-plate capacitor. Correspondingly, the concentration of electric field near the x axis is analogous to the fringe field outside a parallel-plate capacitor.

In Sec. II we have established that the field of the plasmon modes at large distance, $\rho \gg a$, from the origin behaves as $1/\rho$. Hence, the field intensity behaves as $1/\rho^2$; i.e., it strongly diverges down to the distances $\sim a$. This, however, does not translate into a strong enhancement of the *net* energy, $\int d\mathbf{r} \mathbf{E}^2(\mathbf{r})$, which grows only logarithmically, $\propto \ln(\lambda/a)$; the

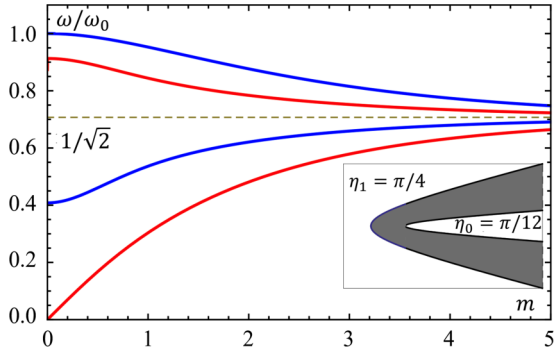


FIG. 9. Illustration of the plasmon spectrum in the geometry of two codirected hyperbolas. Blue and red curves correspond to symmetric and antisymmetric plasmon modes, respectively. The spectrum is plotted from Eq. (34) for $\eta_c = \delta\eta = \pi/6$.

upper cutoff is provided by the wavelength of light, $\lambda = 2\pi c/\omega$, with the same frequency ω .

C. Two codirected hyperbolas

For completeness, in this subsection we will analyze the plasmon spectrum in the geometry of two codirected hyperbolas. Assume that the metal occupies the region $\eta_0 < \eta < \eta_1$, while the regions $0 < \eta < \eta_0$ and $\eta_1 < \eta < \pi$ are occupied by air; see the inset in Fig. 9. A straightforward generalization of Eq. (25) gives

$$\frac{\sinh 2m\eta_0 \sinh 2m(\pi - \eta_1)}{4} = \left[\left(\frac{\omega^2}{\omega_0^2} - \frac{1}{2} \right) \sinh m\pi - \frac{1}{2} \sinh m(\pi - 2\eta_0) \right] \times \left[\left(\frac{\omega^2}{\omega_0^2} - \frac{1}{2} \right) \sinh m\pi + \frac{1}{2} \sinh m(\pi - 2\eta_1) \right]. \quad (34)$$

To analyze the plasmon dispersion, we introduce the average opening angle and the “thickness” of the tip,

$$\eta_c = \frac{\eta_0 + \eta_1}{2}, \quad \delta\eta = \eta_1 - \eta_0. \quad (35)$$

An example of the plasmon spectrum with the two codirected hyperbolas is shown in Fig. 9. In this inverted geometry, symmetric and antisymmetric modes interchange, compared with Fig. 8(b). The symmetric branches in the long-wavelength limit are

$$\omega_s^+(0) = \omega_0 \left(\frac{\delta\eta}{\pi} \right)^{1/2}, \quad \omega_s^-(0) = \omega_0. \quad (36)$$

For the upper symmetric mode, $\omega_s^+(0)$, the signs of the oscillating charges on the opposite sides of each “sleeve” are opposite and the electric field lines are confined inside the metal. For this, the dielectric constant of the metal must vanish. For the lower symmetric mode, $\omega_s^-(0)$, the signs of charges on the opposite sides of each sleeve are the same. The field lines mostly stay in the air and do not penetrate into the metal. This, on the other hand, implies that $\varepsilon(\omega)$ is large, and, correspondingly, the frequency of the mode is small, vanishing in the limit of a very thin “coating,” $\delta\eta \rightarrow 0$.

The acoustic mode, generic for multiconnected geometries, is now found in the antisymmetric part of the spectrum, $\omega_a^+(m) \rightarrow 0$ as $m \rightarrow 0$. The second mode,

$$\omega_a^-(0) = \omega_0 \left(1 - \frac{\delta\eta}{\pi} \right)^{1/2}, \quad (37)$$

lies above $\omega_0/\sqrt{2}$ and its frequency increases with decreasing $\delta\eta$.

IV. INTERACTION OF TWO EMITTERS AT THE METAL-AIR SURFACE

Numerous studies have demonstrated that, due to proximity to the metal, the lifetime of the emitter can be dominated by the excitation of the plasmon modes [6–14]. For a metallic nanoparticle plasmons significantly shorten the lifetime when the emitter frequency is close to the frequency of the plasmon dipole ($l = 1$) oscillations. A less trivial finding [13,14] is that the coupling to plasmons can dominate the lifetime when the emitter is located in the proximity to a nanowire with a subwavelength radius in which the plasmon spectrum is continuous. When the emitter is positioned close to the tip, the plasmon-induced shortening of the lifetime is even more pronounced [14]. This is caused by the field enhancement near the tip. In this regard, to calculate the emitter lifetime in a multiconnected plasmonic structure, we can use the same general scheme as developed in the previous studies.

Consider for concreteness a dipole emitter with frequency ω , located at the metal-air interface, and polarized parallel to the interface, as in Fig. 6. The structure of the plasmon spectrum in this calculation is captured by the Green’s function for the electric field,

$$G(\xi, \eta; \xi', \eta'; \omega) = \sum_m \frac{E_\xi(\xi, \eta; m) E_\xi(\xi', \eta'; m)}{\omega - \omega(m)}, \quad (38)$$

where $E_\xi(\xi, \eta; m)$ is the normalized tangential component of the electric field of the plasmonic mode and the summation is taken over all four modes; $\omega(m)$ is the plasmon spectrum found above. The decay rate is proportional to the imaginary part of the diagonal value $G(\xi, \eta; \xi, \eta; \omega)$ taken at the position of emitter. As the summation in Eq. (38) is performed over acoustic as well as optical modes, a spikelike feature occurs in the ω dependence of the decay rate. The origin of this feature is the divergence of the density of the plasmon modes,

$$g^+(\omega) = \frac{1}{\pi} \int_0^{\omega/\sqrt{2}} dm \delta[\omega - \omega^+(m)], \quad (39)$$

near the threshold frequency $\omega_s^+(0)$.

Consider for simplicity a symmetric geometry, $\eta_0 = \eta_1 < \pi/4$. Expanding Eq. (22) at small m , we get

$$\frac{\omega_s^+(m)}{\omega_s^+(0)} \Big|_{m \rightarrow 0} = 1 + \frac{m^2}{3} \left(\frac{\pi}{4} - \eta_0 \right) \left(\frac{\pi}{2} - \eta_0 \right), \quad (40)$$

where $\omega_s^+(0) = (2\eta_0/\pi)^{1/2}$. Substituting Eq. (40) into Eq. (39), one finds

$$g^+(\omega) = \frac{1}{\pi} \left[\frac{3}{\left(\frac{\pi}{4} - \eta_0 \right) \left(\frac{\pi}{2} - \eta_0 \right) \omega_s^+(0) [\omega - \omega_s^+(0)]} \right]^{1/2}. \quad (41)$$

The inverse square-root singularity in the density of states translates into a minimum in the emitter lifetime. A similar minimum is expected near $\omega = \omega_a^+(0)$ and near the bulk plasmon frequency, ω_0 . Near $\omega = \omega_0/\sqrt{2}$ the minimum should be even stronger, since the divergence of the plasmon modes diverges as $|\omega - \omega_0/\sqrt{2}|^{-1}$.

The scheme of calculation of the plasmon-mediated energy transfer between the emitters near the metal-air interface is also well established; see, e.g., Ref. [10] for two emitters near a nanoparticle and Ref. [41] for donor and acceptor above the graphene. Here we emphasize the specifics of this transfer in the geometry of two hyperbolas. In particular, we study how the transfer rate between the red emitter near the tip in Fig. 6 and the blue emitter located on the left hyperbola differs from the transfer rate between the red emitter and the blue emitter located on the right hyperbola, when both blue emitters have the same coordinate, ξ .

Quantitatively, the relation of the two transfer rates is described by the ratio of the tangential components of electric field at the two interfaces. From Eq. (22) we find

$$T = \left(\frac{E_\xi(\eta_0, \omega)}{E_\xi(\eta_1, \omega)} \right)^2 = \left[\frac{B_1 \cosh(m\eta_0) + B_2 \cosh m(\pi - \eta_0)}{B_1 \cosh m(\pi - \eta_1) + B_2 \cosh(m\eta_1)} \right]^2. \quad (42)$$

With the help of the continuity conditions Eqs. (23) and (24) this ratio can be cast in the form

$$T = [\varepsilon(\omega) \tanh(m\eta_1) \sinh m(\eta_0 - \eta_1) + \cosh m(\eta_1 - \eta_0)]^{-2}, \quad (43)$$

where $m(\omega)$ is determined by the dispersion equation (27). In Fig. 10 we plot the factor T as function of frequency for a fixed opening angle of the right hyperbola, $2\eta_0 = 4\pi/5$, and several opening angles of the left hyperbola. Overall, we see that at $\omega = 0$ the geometric factor T rapidly increases with η_1 . This can be understood from the electrostatics of ideal metals. Indeed, at $\omega = 0$ the field does not penetrate into the metal at all. Consequently, the sharper the left hyperbola is, the stronger the field near the left tip becomes, resulting in smaller values of $T(0)$. This, in turn, means that the energy transfer from the red emitter in Fig. 6 to the left blue emitter happens faster than the transfer to the right blue emitter.

We also see that the behavior of $T(\omega)$ is different for small, Fig. 10(a), and large, Fig. 10(b), values of η_1 . When geometrical factor $T(0)$ is small, $T(\omega)$ falls off with frequency, suggesting that the left and right hyperbolas become effectively “disconnected.” To the contrary, for larger starting values $T(0)$, the finite frequency $T(\omega)$ grows with frequency, suggesting that the energy transfer becomes more symmetric. The crossover from decay to growth takes place at $\eta_1 \approx 0.19\pi$. This value can be related to the peculiar behavior of the velocity of the low-frequency plasmon Eq. (28). Namely, this velocity has a minimum as a function of η_1 . By setting $\partial\omega_s^-/\partial\eta_1 = 0$, we find the position of this minimum at

$$\tilde{\eta}_1 = (\pi\eta_0)^{1/2} - \eta_0. \quad (44)$$

For $\eta_0 = 2\pi/5$, Eq. (44) yields $\tilde{\eta}_1 \approx 0.23\pi$, close to the crossover value of η_1 , which corresponds to $\partial T(\omega)/\partial\omega|_{\omega \rightarrow 0} = 0$.

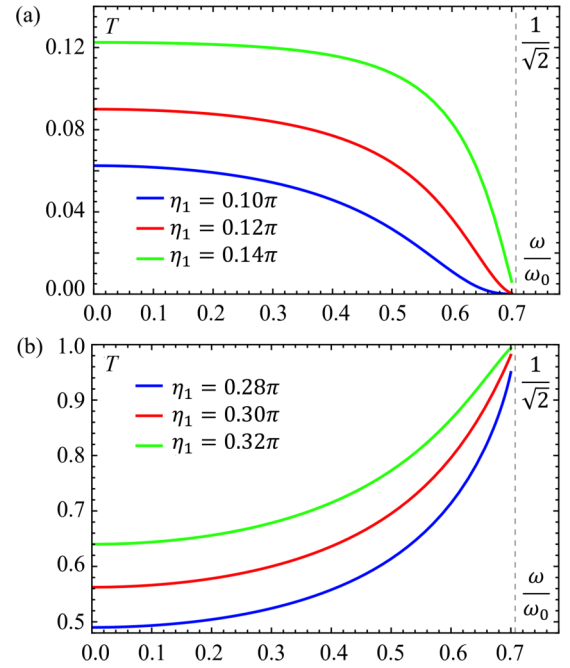


FIG. 10. Geometric factor for the energy transfer is plotted as a function of frequency from Eq. (43) for the values of the opening angle $2\eta_1 = 0.2\pi, 0.24\pi, 0.28\pi$ (a), and $2\eta_1 = 0.56\pi, 0.6\pi, 0.64\pi$ (b). The value of the opening angle, $2\eta_0$, is chosen $2\eta_0 = 4\pi/5$.

It is instructive to discuss Eq. (42) from the general perspective of a resonant energy transfer. Conventionally, the enhancement of the transfer rate between two emitters due to neighboring plane, nanowire, or nanoparticle is studied as a function of the distance between the emitters and the distance from the emitters to the plasmon-guiding interface. For the geometry of two hyperbolas with emitters at the interface, the dependence of the fields on the distance is measured by the dimensionless coordinate ξ . Moreover, this dependence has a purely oscillatory form, $\propto \cos(m\xi)$. Thus, the effectiveness of the resonant energy transfer depends exclusively on the opening angles and the frequency (in the units of ω_0). The most nontrivial outcome of Eqs. (42) and (43) and Fig. 10 is that, at frequency close to the surface plasmon frequency $\omega_0/\sqrt{2}$, the ratio of the transfer rates to “left” and to the “right” switches abruptly from 0 to 1 depending on the relation between the opening angles.

V. CONCLUDING REMARKS

(i) The prime qualitative finding of the present paper is that, for a singly connected geometry, the opening angle of the hyperbola, $2\eta_0$, defines the minimum frequency, given by Eq. (14), below which the plasmon bound to the tip of the hyperbola does not exist. By contrast, in a multiconnected geometry a symmetric plasmon mode, concentrated near the region of the closest contact of the surfaces, exists at arbitrary low frequency.

(ii) A geometry somewhat similar to the one considered in this paper was studied in Refs. [42–46]. The authors considered two or more plasmonic wires or radius a in parallel and separated by distance d . They traced numerically how

plasmons of individual wires hybridize with decreasing d . For the case in which both a and d are much less than the wavelength, the expected distribution of the field is a universal function of the ratio d/a . However, for the parameters of interest the retardation effects were important. In the exact solution found in this paper it is not possible to incorporate the retardation effects. Understandably, this limitation restricts the applicability of our analytical results to the domain of small enough wavelength or large momenta m (see below).

(iii) Originally, the enhancement of the electric field of a plasmon-polariton as it approaches a wedge has been demonstrated analytically in Ref. [15]. Calculation in Ref. [15], was carried out in polar coordinates, i.e., neglecting the rounding of the wedge near the tip. This curving has been emulated by introducing a cutoff length $\sim a$. At distances much greater than a the form of the plasmon field in Ref. [15] is consistent with Eq. (16) with the important difference that the plasmon field Eq. (16) is not traveling, as in Ref. [15], but is a standing wave instead. This structure is enforced by the boundary condition at the tip.

The fact that the plasmon mode near the tip is a standing wave can be viewed from the perspective of focusing of light on a subwavelength scale, when the plasmon-polariton with TM polarization (magnetic field along the z axis) is excited at large (compared to the wavelength, λ) distance, ρ , from the tip [18]. In the geometry of a single hyperbola this polariton will be fully reflected. For small enough opening angles, $2\eta_0$, the transformation of the polariton into small- ρ standing plasmon mode can be traced analytically within the semiclassical (WKB) description [13,14,18–20,22]. Within that description, the metal strip at distances $\rho \gg a$ from the origin is replaced with a planar film with a thickness d_ρ , equal to the arc distance, $2\rho\eta_0 = d_\rho$, between the two metal surfaces. Then the semiclassical expression for the incident and reflected fields has the form $q_\rho^{-1/2} \exp[\pm i \int d\rho q_\rho]$, where $q_\rho(\omega)$ is the dispersion of the symmetric waveguide mode propagating along the film. This dispersion law satisfies the equation

$$\varepsilon \tanh \left\{ \left(q_\rho^2 - \varepsilon \frac{\omega^2}{c^2} \right)^{1/2} \frac{d_\rho}{2} \right\} = - \left(\frac{q_\rho^2 - \varepsilon \frac{\omega^2}{c^2}}{q_\rho^2 - \frac{\omega^2}{c^2}} \right)^{1/2}. \quad (45)$$

The relevant question is, how close to the threshold frequency $\omega_0(\eta_0/\pi)^{1/2}$ is the semiclassical description applicable, i.e., when does the condition $dq_\rho/d\rho \ll q_\rho^2$ apply? At small frequencies we can replace $\varepsilon(\omega)$ by $-\omega_0^2/\omega^2$ and simplify Eq. (45) using the identification $q_\rho = m/\rho$, Eq. (17). Then Eq. (45) reduces to the following equation for m :

$$\tanh \left[\eta_0 m \left(1 + \frac{\omega_0^2 \rho^2}{c^2 m^2} \right)^{1/2} \right] = \frac{\omega^2}{\omega_0^2} \left(1 + \frac{\omega_0^2 \rho^2}{c^2 m^2} \right)^{1/2}, \quad (46)$$

and the semiclassical condition is satisfied provided that $m \gg 1$. As the distance ρ increases, the solution of Eq. (46) grows starting from $m = \frac{\omega^2}{\omega_0^2 \eta_0}$, which is consistent with Eq. (11). Thus, for the semiclassical description to apply at all ρ bigger than a , it is necessary that this minimum m exceeds 1, i.e., $\omega \gg \omega_0 \eta_0^{1/2}$. The latter condition suggests that the frequency of the incident light, being much smaller than ω_0 , should still not be very close to the threshold frequency.

Another approach to the “delivery” of the light energy to the tip was proposed in Ref. [21]. Namely, one can coat a conical tip of a glass fiber by a silver layer, the geometry similar to the one shown in the inset in Fig. 9. The wavelength of a plasmon in a silver layer increases away from the tip, and at a certain distance matches the wavelength of the waveguided light propagating towards the tip. At this point the light transforms into the plasmon and heads towards the tip. Experimental realization of a coupling based on this idea was reported in a number of papers; see Ref. [37] and references therein.

(iv) Naturally, the structure of the plasmon field at small distances from the tip is not captured in polar coordinates. Meanwhile, this structure is quite nontrivial. To illustrate this, consider the ratio $E_x(0)/E_{x,\text{tip}}$ of the fields at the origin and at the tip for a symmetric plasmon. This ratio can be found from Eq. (19). The origin, $x = 0$, corresponds to $\eta = \pi/2$, while the tip corresponds to $x = a \cos \eta_0$. Then Eq. (19) yields

$$\frac{E_x(0)}{E_{x,\text{tip}}} = \frac{\sin \eta_0 \sinh \left[\frac{\pi}{2} m(\omega) \right]}{\sinh[(\pi - \eta_0)m(\omega)]}. \quad (47)$$

As the frequency grows from the threshold value $\omega_s(0) = \omega_0(\eta_0/\pi)^{1/2}$ to the surface plasmon frequency $\omega_0/\sqrt{2}$, the “wave number,” m , changes from $m = 0$ to $m = \infty$. Then the ratio Eq. (47) falls off from $\pi \sin \eta_0/[2(\pi - \eta_0)]$ monotonically. At frequencies close to $\omega_0/\sqrt{2}$ the ratio Eq. (47) approaches zero, since the plasmon field is strongly localized near the metal surface. Such a strong change of the field is revealed by the exact solution in elliptic coordinates demonstrated in the present paper.

(v) In this paper we assumed that the plasmon field does not depend on z . For a general z dependence, $\Phi \propto \exp(i\kappa z)$, the Laplace equation takes the form

$$\frac{\partial^2 \Phi}{\partial \xi^2} + \frac{\partial^2 \Phi}{\partial \eta^2} + \kappa^2 a^2 (\cosh^2 \xi - \cos^2 \eta) \Phi = 0. \quad (48)$$

Separation of variables leads to the following equation for the potential's η dependence,

$$\frac{\partial^2 \Phi}{\partial \eta^2} - (m^2 + \kappa^2 a^2 \cos^2 \eta) \Phi = 0. \quad (49)$$

Our results apply for the wave numbers that exceed some minimum value, $m \gg m_{\min}$. This minimum value can be estimated from the observation that κ cannot be less than H^{-1} , where H is the “height” of the hyperbola; see Fig. 1. This determines $m_{\min} \sim \kappa a \sim a/H \ll 1$.

(vi) A finite scattering rate of conduction electrons, γ , sets the maximum distance from the origin, ρ_{\max} , where our results apply. The solutions obtained and discussed above decay beyond ρ_{\max} . This distance can be estimated by noting that a finite γ is taken into account by replacing $\omega^2 \rightarrow \omega(\omega + i/\gamma)$ in the dielectric function, Eq. (2). As a result, it leads to a finite imaginary part of m : $\text{Im } m \approx \gamma(\partial\omega/\partial m)^{-1}$, where $\partial\omega/\partial m$ is the slope of the plasmon dispersion. The plasmons attenuate at distances where $\xi \text{Im } m \sim 1$. Since at large distances ξ depends logarithmically on ρ , see Eq. (16), we conclude that the maximum distance is $\rho_{\max} \sim a \exp[1/\text{Im } m]$.

(vii) Finally, throughout the paper, we have disregarded the spatial dispersion of the dielectric permittivity, $\varepsilon(\omega, k) \approx \varepsilon(\omega)$.

Such approximation is valid as long as the characteristic wave vectors k are small: $k \ll \omega_0/v$, where v is the electron Fermi velocity [47,48]. Using the value of the plasma frequency for gold [49] $\omega_0 = 1.38 \times 10^{16} \text{ s}^{-1}$, and its Fermi velocity [50] $v = 1.39 \times 10^8 \text{ cm/s}$, we obtain the value of the wave vector for which spatial dispersion must be taken into account, $k_0 \sim 10^8 \text{ cm}^{-1}$. On the other hand, the smallest wave vector in our wedge geometry is determined by the radius of curvature of the hyperbolas near their sharp points, $k \sim 2\pi/a$. We,

therefore, conclude that for $a \gtrsim 1 \text{ nm}$, neglecting spatial dispersion should be a good approximation.

ACKNOWLEDGMENTS

L.S. and E.M. were supported by the Department of Energy, Office of Basic Energy Sciences, Grant No. DE-FG02-06ER46313. M.R. was supported by the NSF MRSEC program at the University of Utah under Grant No. DMR 1121252.

-
- [1] J. A. Schuller, E. S. Barnard, W. Cai, Y. C. Jun, J. S. White, and M. L. Brongersma, *Nat. Mater.* **9**, 193 (2010).
- [2] D. K. Gramotnev and S. I. Bozhevolnyi, *Nat. Photonics* **4**, 83 (2010).
- [3] Z. Han and S. I. Bozhevolnyi, *Rep. Prog. Phys.* **76**, 016402 (2013).
- [4] D. K. Gramotnev and S. I. Bozhevolnyi, *Nat. Photonics* **8**, 13 (2013).
- [5] M. I. Stockman, *Science* **348**, 287 (2015).
- [6] P. Andrew and W. L. Barnes, *Science* **306**, 1002 (2004).
- [7] P. Anger, P. Bharadwaj, and L. Novotny, *Phys. Rev. Lett.* **96**, 113002 (2006).
- [8] S. Kuhn, U. Hakanson, L. Rogobete, and V. Sandoghdar, *Phys. Rev. Lett.* **97**, 017402 (2006).
- [9] O. L. Muskens, V. Giannini, J. A. Sánchez-Gil, and J. Gómez Rivas, *Nano Lett.* **7**, 2871 (2007).
- [10] A. O. Govorov, J. Lee, and N. A. Kotov, *Phys. Rev. B* **76**, 125308 (2007).
- [11] V. N. Pustovit and T. V. Shahbazyan, *Phys. Rev. Lett.* **102**, 077401 (2009).
- [12] E. G. Mishchenko, *Phys. Rev. B* **88**, 115436 (2013).
- [13] D. E. Chang, A. S. Sørensen, P. R. Hemmer, and M. D. Lukin *Phys. Rev. Lett.* **97**, 053002 (2006).
- [14] D. E. Chang, A. S. Sørensen, P. R. Hemmer, and M. D. Lukin, *Phys. Rev. B* **76**, 035420 (2007).
- [15] K. V. Nerkararyan, *Phys. Lett. A* **237**, 103 (1997).
- [16] J. Takahara, S. Yamagishi, H. Taki, A. Morimoto, and T. Kobayashi, *Opt. Lett.* **22**, 475 (1997).
- [17] A. J. Babadjanyan, N. L. Margaryan, and K. V. Nerkararyan, *J. Appl. Phys.* **87**, 3785 (2000).
- [18] M. I. Stockman, *Phys. Rev. Lett.* **93**, 137404 (2004); **106**, 019901(E) (2011).
- [19] D. K. Gramotnev, *J. Appl. Phys.* **98**, 104302 (2005).
- [20] M. V. Vogel and D. K. Gramotnev, *Phys. Lett. A* **363**, 507 (2007).
- [21] N. A. Janunts, K. S. Baghdasaryan, K. V. Nerkararyan, and B. Hecht, *Opt. Commun.* **253**, 118 (2005).
- [22] D. K. Gramotnev, M. W. Vogel, and M. I. Stockman, *J. Appl. Phys.* **104**, 034311 (2008).
- [23] A. Rusina, M. Durach, K. A. Nelson, and M. I. Stockman, *Opt. Express* **16**, 18576 (2008).
- [24] K. Kurihara, J. Takahara, K. Yamamoto, and A. Otomo, *J. Phys. A: Math. Theor.* **42**, 185401 (2009).
- [25] K. Kurihara, A. Otomo, K. Yamamoto, J. Takahara, M. Tani, and F. Kuwashima, *Plasmonics* **10**, 165 (2014).
- [26] J. Mao and S. Blair, *J. Phys. D: Appl. Phys.* **48**, 184008 (2015).
- [27] E. Verhagen, A. Polman, and L. K. Kuipers, *Opt. Express* **16**, 45 (2008).
- [28] V. Astley, R. Mendis, and D. M. Mittleman, *Appl. Phys. Lett.* **95**, 031104 (2009).
- [29] D. M. Mittleman, *Nat. Photonics* **7**, 666 (2013).
- [30] W. Srituravanich, L. Pan, Y. Wang, C. Sun, D. B. Bogy, and X. Zhang, *Nat. Nanotechnol.* **3**, 733 (2008).
- [31] G. Vecchi, V. Giannini, and J. Gómez Rivas, *Phys. Rev. B* **80**, 201401(R) (2009).
- [32] T. Zhang, S. Callard, C. Jamois, C. Chevalier, D. Feng, and A. Belarouci, *Nanotechnology* **25**, 315201 (2014).
- [33] H. Kollmann, X. Piao, M. Esmann, S. F. Becker, D. Hou, C. Huynh, L.-O. Kautschor, G. Bösker, H. Vieker, A. Beyer, A. Götzhäuser, N. Park, R. Vogelgesang, M. Silies, and C. Lienau, *Nano Lett.* **14**, 4778 (2014).
- [34] M. G. Nielsen and S. I. Bozhevolnyi, *J. Opt. Soc. Am. B* **32**, 462 (2015).
- [35] M. Kauranen and A. V. Zayats, *Nat. Photonics* **6**, 737 (2012).
- [36] S.-W. Qu and Z.-P. Nie, *Sci. Rep.* **3**, 3172 (2013).
- [37] H. Gao, Q. Cao, M. Zhu, D. Teng, and S. Shen, *Opt. Express* **22**, 32071 (2014).
- [38] F. Stern, *Phys. Rev. Lett.* **18**, 546 (1967).
- [39] I. V. Novikov and A. A. Maradudin, *Phys. Rev. B* **66**, 035403 (2002).
- [40] E. Moreno, S. G. Rodrigo, S. I. Bozhevolnyi, L. Martín-Moreno, and F. J. García-Vidal, *Phys. Rev. Lett.* **100**, 023901 (2008).
- [41] K. A. Velizhanin and T. V. Shahbazyan, *Phys. Rev. B* **86**, 245432 (2012).
- [42] A. Manjavacas and F. J. Garcia de Abajo, *Nano Lett.* **9**, 1285 (2009).
- [43] A. Manjavacas and F. J. Garcia de Abajo, *Opt. Express* **17**, 19401 (2009).
- [44] Z.-X. Zhang, M.-L. Hu, K. T. Chan, and C.-Y. Wang, *Opt. Lett.* **35**, 3901 (2010).
- [45] V. Myroshnychenko, A. Stefanski, A. Manjavacas, M. Kafesaki, R. I. Merino, V. M. Orera, D. A. Pawlak, and F. J. Garcia de Abajo, *Opt. Express* **20**, 10879 (2012).
- [46] S. Sun, H.-T. Chen, W.-J. Zheng, and G.-Y. Guo, *Opt. Express* **21**, 14591 (2013).
- [47] E. M. Lifshitz and L. P. Pitaevskii, *Physical Kinetics* (Butterworth-Heinemann, Oxford, 1997).
- [48] I. A. Larkin, M. I. Stockman, M. Achermann, and V. I. Klimov, *Phys. Rev. B* **69**, 121403(R) (2004).
- [49] L. Novotny and B. Hecht, *Principles of Nanooptics* (Cambridge, New York, 2006).
- [50] Ch. Kittel, *Introduction to Solid State Physics* (John Wiley & Sons, Hoboken, 2005).